JOURNAL OF GUIDANCE, CONTROL, AND DYNAMICS
Vol. 28, No. 6, November–December 2005

Longitudinal H_∞ Stability Augmentation System for a Thrust-Vectored Unmanned Aircraft

N. Kannan* and M. Seetharama Bhat†
Indian Institute of Science, Bangalore 560 012, India

The development of discrete longitudinal H_∞ stability augmentation system to improve the handling qualities of a radio-controlled unmanned aircraft is presented. The aircraft features thrust-vector control by deflection of a cold jet to expand the operating envelope. Output sensitivity and a control sensitivity minimization problem are considered to suppress low-frequency gust disturbance and high-frequency noise disturbance and to ensure proper control allocation between the elevator and the thrust flap. Gain scheduling is avoided by designing a single controller at the operating point most sensitive to perturbations in actuators and the aerodynamic model. To this end, a systematic method to choose the design operating point is presented. The closed-loop system is comprehensively tested for robust stability using μ analysis and for robust performance over the entire cruise envelope. Disturbance and sensor noise rejection capabilities are assessed for realistic gust and sensor noise using nonlinear simulation and hardware in loop simulation. The entire design procedure is performed in discrete time.

I. Introduction

THE development of thrust vector control (TVC) is necessitated by the rigorous demands of modern military aviation. These demands are difficult, if not impossible, to be met using conventional control surfaces because of loss of control effectiveness at low speeds due to low dynamic pressure. They are also ineffective in the poststall flight regime.[1,2] Many experimental flight vehicles like the Highly Maneuverable Aircraft Technology (HiMAT[3]) have been developed in an attempt to expand the flight envelope of modern aircraft. In this context, a radio-controlled miniature combat aircraft, research aircraft (RA) is developed at the Department of Aerospace Engineering, Indian Institute of Science, to study the effectiveness of TVC at low speeds.[4] Flying of these low-inertia aircraft through joystick-driven ground command, based on visual cues, becomes easier due to the fast damped response of controlled airframe. Apart from improving the handling qualities of the vehicle, the proposed stability augmentation system (SAS) is expected to provide better control authority to the elevator than the thrust flap, yet keep the thrust flap operational and effective.

One of the challenges in the development of such an aircraft is the design of robust flight controllers, because the aircraft dynamics vary substantially throughout the flight envelope. H_∞ control presents an attractive option among multivariable methods for SAS design because multivariable robustness measures can be incorporated directly into the optimization criterion. Hyde[5] uses the loop-shaping/H_∞ approach for the design of a flight controller for a vertical and/or short takeoff and landing aircraft. H_∞ inner-/outer-loop structure is designed for a thrust-vectored aircraft at a single flight condition in Ref. 6. Adams et al.[7] present the design of a controller by μ synthesis for robust stability and performance over the full flight envelope at high angle of attack using an inner-/outer-loop approach. Dynamic inversion/μ synthesis inner-/outer-loop control is used for a thrust-vectored F-18 by Adams et al.[8] and for a thrust-vectored F-16 by Reigelsperger and Banda.[9] Tucker and Walker[10] use a model matching inner-/outer-loop H_∞ approach to the design of a robust flight controller for a research civil aircraft. A discrete-time H_∞ controller is designed for the longitudinal dynamics of RA at a single flight condition in Ref. 11.

Another aspect of aircraft control is gain scheduling or switching of controllers. However, scheduling of controllers introduces many complexities at the stage of implementation, such as switching between controllers and the need for additional measurements such as speed and altitude for gain scheduling. Designing a single controller that can provide simultaneous stabilization in the entire operating range of flight can overcome such constraints. Shin et al.[12] use the worst-case algorithm to determine the flight condition most sensitive to perturbations for the lateral dynamics of an X-38, and it is shown that the controller designed at this operating point performs satisfactorily at other flight conditions. A similar approach is used in the present work for the choice of an operating point for controller design. The discrete-time longitudinal controller is designed using the algorithm in Ref. 13 and is implemented for RA on an onboard computer.

Whereas the majority of the references on the design of robust controllers for aircraft are with respect to full-scale aircraft, little attention has been devoted to the low-cost unmanned aerial vehicles (UAVs). The small size and inertia of UAVs make them more highly susceptible to wind gusts than conventional aircraft. The uncertainties associated with low-Reynolds-number flight (typical for low-speed UAVs) are not fully understood and are significant. The main contribution of this paper is the incorporation of well-established discrete H_∞ control theory[13] in the design of a robust longitudinal flight controller that meets flight stabilization and performance requirements for all flight speeds, without scheduling and validation through hardware-in-loop-simulation (HILS), for a thrust-vectored, low-speed aircraft remotely controlled from the ground.

The organization of the paper is as follows: An RA model and thrust-vectoring scheme is described briefly in Sec. II, including pole locations for straight and level flight conditions covering the entire cruise speed range. In Sec. III, the SAS specifications and the selection of the best operating speed for controller design are described. H_∞ controller synthesis using the algorithm from Ref. 13 is presented in Sec. IV. The closed-loop system performance and stability robustness are also analyzed at all flight conditions in this section. Simulation results using a nonlinear model and HILS are presented in Sec. V.

II. RA Configuration and Mathematical Model

A. Configuration

The RA configuration shown in Fig. 1 is chosen to represent a typical combat aircraft. RA is a delta-wing low-inertia aircraft without a horizontal tail and with a takeoff weight of approximately

Received 14 August 2004; revision received 10 December 2004; accepted for publication 13 December 2004.

*Research Scholar, Department of Aerospace Engineering; nkannan@aero.iisc.ernet.in.

†Professor, Department of Aerospace Engineering; msbdcl@aero.iisc.ernet.in.

Fig. 1 Research aircraft and thrust flap arrangement.

5.5 kg. It is powered by a ducted fan driven by a 15-cm^3 piston engine (OS91) with achievable revolutions per minute of approximately 18,000. The fuel is a mixture of methanol and castor oil with nitromethane added to boost the power. The aircraft is controlled through inboard and outboard elevons on the wing, thrust flap, and rudder on the vertical tail. A simple but effective approach of tilting a flap (paddle) at the end of the exhaust duct to deflect a cold jet is used for thrust vectoring. Experimental results obtained from wind tunnel studies show that 1 deg of thrust flap deflection is equivalent to 0.7 deg of elevator deflection.[14] Because the model is flown remotely from ground, it is designed to be inherently stable, with a static margin of 6% (of mean geometric chord), that is, the center of gravity is at a distance of 0.048 m ahead of the neutral point or aerodynamic center (where the coefficient of pitching moment is independent of angle of attack). The various parameters of RA are given in the Appendix.

B. Mathematical Model

The cruise speed range of RA is 25–45 m/s. Because the flight altitude does not vary significantly, density variations are neglected, and the vehicle is assumed to cruise at 1200 m, that is, 300 m above Bangalore, India, height. The longitudinal dynamics of the aircraft in matrix form after linearization around a trim condition is[15]

$$\begin{bmatrix} \dot{u} \\ \dot{\alpha} \\ \dot{q} \\ \dot{\theta} \end{bmatrix} = \begin{bmatrix} X_u & X_\alpha & 0 & -g \\ Z_u/U & Z_\alpha/U & (Z_q+U)/U & 0 \\ M_u & M_\alpha & M_q & 0 \\ 0 & 0 & 1 & 0 \end{bmatrix} \begin{bmatrix} u \\ \alpha \\ q \\ \theta \end{bmatrix} + \begin{bmatrix} X_{\delta e} & X_{\delta t} \\ Z_{\delta e}/U & Z_{\delta t}/U \\ M_{\delta e} & M_{\delta t} \\ 0 & 0 \end{bmatrix} \begin{bmatrix} \delta_e \\ \delta_t \end{bmatrix} \tag{1}$$

where u is the change in forward velocity, g is the acceleration due gravity, θ is the change in pitch angle, α is the change in angle of attack, δ_e is the change in elevator deflection, q is the pitch rate, and δ_t is the thrust flap deflection. U is the trim velocity. The aircraft is trimmed for level flight at speeds of 25, 30, 35, 40, and 45 m/s. Because the aircraft uses electromechanical servoactuators (Futaba 3003), the input to the actuator is a pulse width modulator (PWM) signal with a pulse repetition frequency of 50 Hz, and the PWM signals are generated using a motor control digital signal processor (DSP) from Texas Instruments (TMS320LF2407A). Hence, the input control variable is a PWM pulse width. The elevator and thrust flap actuators (electromechanical) are modeled as first-order dynamic systems with the continuous-time transfer function obtained experimentally (output deflection in radians and input in milliseconds of pulse width):

$$\delta_t/\delta_c = \delta_e/\delta_c = K_a/(T_a s + 1) \tag{2}$$

where $K_a = 0.671$ and actuator time constant $T_a = 0.105$ s. The measured outputs are q and a_z, and the command signals from ground are demands on the normal acceleration a_z. The relation for normal acceleration is

$$a_z = U(\dot{\alpha} - q) + l_v \dot{q} \tag{3}$$

where l_v is the distance of rate gyroscope and accelerometer location from the c.g. and $l_v = 0.47$ m. The accelerometer (TAA-3104-100, from NeuwGhent Technology) sensitivity is 0.5 V/g and rate gyro (Microgyro 100 from GYRATION, Inc.) sensitivity is 1.2721 V/rads^{-1}, inclusive of the preamplifier gain in the flight instrumentation.

The elements of coefficient matrices in Eq. (1) are termed stability and control derivatives. Stability derivatives can be further classified into static and dynamic derivatives. Static derivatives are the dimensional variation of forces and moments with respect to aerodynamics and motion variables, whereas dynamic derivatives are dimensional variations of forces and moments with respect to rate of change of aerodynamics and motion variables.

The static derivatives are obtained from static, low-speed wind-tunnel tests because they are more accurate than analytical means (DATCOM[16]). However, estimation of dynamic derivatives using an oscillatory rig in a wind tunnel is complex, hence, they are found using DATCOM. Note that Eq. (1) does not contain dynamic derivatives due to $\dot{\alpha}$ because of the absence of horizontal tail. Though this may be detrimental in terms of reduced short-period damping,[15] the removal of a horizontal tail helps in reduced overall weight and increased endurance. The thrust flap control derivatives in Eq. (1) are derived from the incremental lift, drag, and moment equations that are modeled as a function of exit momentum of the jet, duct area, distance of exit duct from the c.g., and the distance of air intake from c.g. Ideally, for aircraft flying over a wide operating envelope, the exit momentum varies inversely with speed. The exit momentum stays nearly constant at 26.5 N for RA over the cruise range; therefore, the thrust flap effectiveness is expected to remain constant for all cruise speeds. The state-space model for the representative case of 45 m/s is given in the Appendix, as are the trim parameters for straight and level flight at different speeds. The longitudinal mode natural frequencies and damping at these speeds are given in Table 1.

Table 1 Open- and closed-loop phugoid and short-period frequency and damping

Speed, m/s	Open-loop frequency, rad/s	Open-loop damping	Closed-loop frequency, rad/s	Closed-loop damping
25	0.494	0.131	0.573	0.48
	6.44	0.475	6.39	0.49
30	0.412	0.15	0.46	0.52
	7.76	0.48	7.75	0.497
35	0.353	0.18	0.343	0.56
	9.06	0.48	9.08	0.495
40	0.309	0.227	0.25	0.6
	10.3	0.479	10.4	0.49
45	0.275	0.274	0.215	0.63
	11.6	0.477	11.7	0.488

III. Flight-Control System Specifications and Operating Point Selection for Controller Design

A. Specifications

The closed-loop design specifications mainly concern gust disturbance rejection, sensor noise rejection, and robustness to variation in speed within the operating envelope and model uncertainty. Though flying qualities specifications are not available for subscale aircraft, such specifications for piloted aircraft can act as a guideline with respect to which design can be used.[17] For full-scale aircraft, flying qualities evaluation is performed through pilot-opinion rating scales such as the Cooper–Harper scale.[18] Accordingly, the U.S.

military specifications[19] for level-1 flying qualities (excellent aircraft characteristics and pilot compensation not a factor for desired performance) state that the phugoid ξ_p and short-period ξ_{SP} damping requirements are

$$\xi_p \geq 0.5 \tag{4}$$

$$0.35 < \xi_{SP} < 1.3 \tag{5}$$

It can be seen from Table 1 that, though the short-period damping is low, criterion (5) is satisfied, but the phugoid damping is lower than the specification. Therefore, the phugoid mode damping has to be improved to meet the flying quality requirement. With reference to Table 1, it can be seen that the short-period dynamics is fast due to low inertia. Because this is desirable, the closed-loop characteristics, in terms of speed of response, should not be significantly lower than open loop. The aim is to design an SAS to achieve good maneuverability; hence, the command signals from ground are demands on a_z. However, zero steady-state error in tracking a_z is not important because the pilot can compensate for loss in a_z manually through joystick movement.

1. Gust Disturbance Rejection

Atmospheric turbulence is a low-frequency phenomenon that commonly occurs during flight and that can have an adverse effect on the response of aircraft, especially for a subscale aircraft due to its high susceptibility to turbulence. To determine the gust rejection specifications of the closed-loop system, the vertical wind gust noise is taken to have a spectral density given in Dryden form (see Ref. 20) as

$$\Phi_w(\omega) = \frac{2L_w\sigma^2}{\pi U}\,\frac{1 + 12(L_w/U)^2\omega^2}{\left(1 + 4(L_w/U)^2\omega^2\right)^2} \tag{6}$$

where ω is the frequency in radian per second, σ is the turbulence standard deviation, L_w is the turbulence scale length, and U is the flight velocity. The turbulence scale length at 1200-m altitude is[20]

$$L_w = 265 \text{ m} \tag{7}$$

The turbulence standard deviations are defined in statistical terms and classified as light, severe, and moderate, with $\sigma = 1.55$ m/s for light wind, $\sigma = 3.05$ m/s for moderate wind, and $\sigma = 5.96$ m/s for severe wind conditions.[19] Given that RA is usually flown in mild or calm wind conditions, a standard deviation of 2.5 m/s is chosen. The gust spectral density at different speeds is given in Fig. 2. The frequency range of concentration of gust disturbance is found to increase with speed and reaches 13 rad/s for the flight condition at 45 m/s. This represents the worst-case scenario when disturbances may excite both the phugoid and short-period modes. When this is used as the benchmark, the gust rejection specification is to reject all disturbances below 13 rad/s.

2. Noise Rejection

Though the microelectromechanical systems sensors have an inbuilt 50-Hz low-pass filter, it is found that the sensor outputs are noisy and biased, with noise concentration in the region above 30 rad/s, which makes the control of aircraft difficult. Thus, the high-frequency specification is to reject all noise above 30 rad/s.

3. Robustness Requirements

The controller designed at the worst-case operating condition should be robust to variations in flight conditions. It should also be robust to structured uncertainty in plant models and unstructured multiplicative uncertainties at actuator inputs that are present at all flight conditions. Structured uncertainty in plant models stems from the confidence level reposed in various aerodynamic derivatives. In general, data from wind tunnels are more reliable than those calculated from analytical means, and, hence, a larger uncertainty level is placed on dynamic derivatives. Thus, the uncertainties in dimensional derivatives are X_u, 20%; X_α, 10%; Z_q, 10%; M_α, 25%; M_q, 20%; $Z_{\delta e}$, 20%; $Z_{\delta t}$, 20%; $M_{\delta e}$, 20%; and $M_{\delta t}$, 20%. These uncertainty values are assumed constant at all flight conditions. Unstructured uncertainties in elevator and thrust flap actuators are assumed to be in the input multiplicative form and are weighted by the transfer matrix

$$W_{\text{act}} = [(s + 2.5)/(s + 50)]I_{2\times 2} \tag{8}$$

This implies a low-frequency error of 5%, which increases with frequency up to 100%. Quantitatively, the μ bounds of the closed-loop system should be less than one at all flight conditions for the uncertainty range just described. The closed-loop system should also be robust to nominal expected onboard computational time delays of 0.02 s. (Control input at the present sampling instant is based on the sensor outputs measured at the preceding sampling instant.)

Apart from the preceding specifications, the maximum control surface deflection should not exceed the experimentally determined limits of ±15.7 and ±16.3 deg for the elevator and thrust flap, respectively.

B. Operating Point Selection for Controller Design

The main aim of the present work is to design a single controller for the entire flight range to achieve the simultaneous stabilization, disturbance rejection, and noise rejection requirements just outlined. Figure 3 shows the singular value plot of the open-loop frequency response at different operating speeds. Figure 3 shows that the frequency response shapes are similar due to small changes in cruise speed. However, the difference in maximum singular values is largest between the open-loop plants at 45 and 25 m/s. This difference varies from 6.5 dB in the frequency range of 0.1–10 rad/s to 10 dB above 10 rad/s. It is obvious that the gain difference is high between the extreme operating points, which calls for a robust

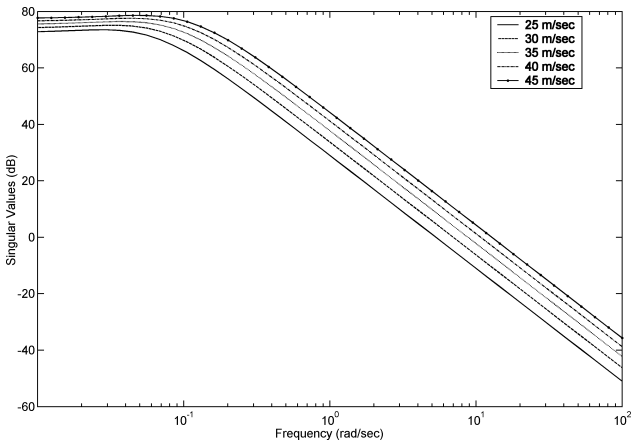

Fig. 2 Frequency response of wind spectral density for different flight speeds.

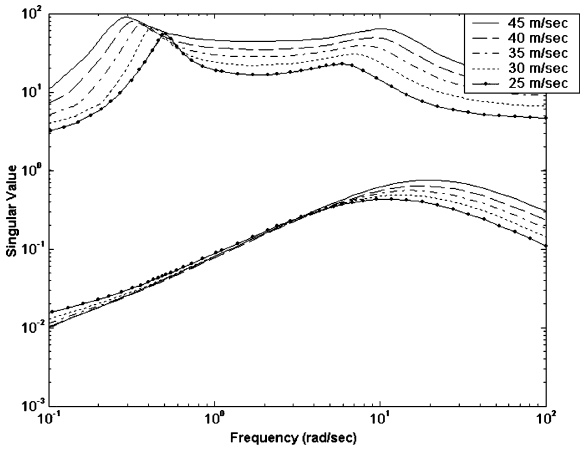

Fig. 3 Singular value plot of open-loop frequency responses at different flight conditions.

controller. However, in addition to stability robustness, performance preservation is also an important requirement for controller design as mentioned earlier. Hence, the design operating point should have minimal robustness requirements so that the design is not conservative with respect to performance. Two criteria are outlined here for choosing the design operating point:

1. Criterion 1

Denote the prospective plant model for controller design as G_{o1} and the plant models at other flight conditions as G_i, where $i = 1{:}4$, because there are five operating points. The other operating points G_i can then be treated as perturbations away from the prospective operating point G_{o1}, and the best operating point is the one at which the magnitude of perturbation ratio $\bar{\sigma}[(G_i - G_{o1})/G_{o1}]$ is at a minimum over all G_{o1} in the frequency range that includes both the short-period and phugoid modes, that is, the best operating point G_o satisfies the following condition:

$$\max_{G_i} \bar{\sigma}[(G_i - G_o)/G_o] \leq \max_{G_{o1}} \max_{G_i} \bar{\sigma}[(G_i - G_{o1})/G_{o1}] \qquad (9)$$

Equation (9) basically means that the best operating point G_o is nearer to all other flight conditions than any other operating point, thereby minimizing the requirement on robustness.

2. Criterion 2 (Worst-Case Criterion)[12,21]

The effects of the uncertain aerodynamic derivatives on the open-loop plant model also play an important role in the determination of the best operating point. Controller design at the operating point most sensitive to perturbations helps in avoiding overemphasis on stability to perturbations at other flight conditions, thereby resulting in better performance.

Consider the perturbation set $\mathbf{\Delta}_p$ corresponding to real parameter uncertainties and complex unstructured uncertainties of the open-loop transfer function matrix G_o (Fig. 4). $\mathbf{\Delta}_p$ has a diagonal structure with scalar real and complex elements. The worst-case perturbation set Δ_ω for G_o at each frequency ω is defined as

$$\left\{\Delta_\omega \in \mathbf{\Delta}_p : \max_{\Delta \in \Delta_p} \bar{\sigma}[G(\Delta)|_\omega - G_o|_\omega]\right\} \qquad (10)$$

where the subscript ω represents the frequency at which the worst-case perturbation set is evaluated. $G_o|_\omega$ is the nominal open-loop transfer function evaluated at the frequency ω, and $G(\Delta)|_\omega$ is the perturbed open-loop transfer function evaluated at ω. In the present case, there are no complex perturbations because the nominal actuator transfer function is assumed to be invariant at all flight conditions. Therefore, $\mathbf{\Delta}_p$ takes the form

$$\mathbf{\Delta}_p := \text{diag}(\delta_1, \delta_2, \ldots, \delta_9), \; -1 \leq \delta_i \leq 1 \qquad (11)$$

corresponding to the nine uncertain aerodynamic derivatives. The maximization problem of Eq. (10) is basically a problem of finding the perturbation that results in a perturbed plant model most distant from the nominal open-loop plant. Once the worst-case perturbations are calculated, the uncertainty ratio $|[G(\Delta_\omega) - G_o|_\omega]/G_o|_\omega|$ can be found for all operating points at all frequencies. The flight condition with the largest uncertainty ratio is then the operating point most sensitive to perturbations, and controller design can be performed at this point.

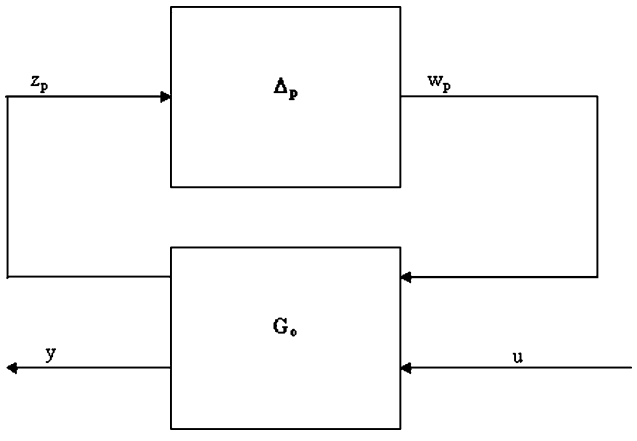

Fig. 4 Interconnection for worst-case analysis problem.

For the purpose of calculating Δ_ω, a worst-case analysis is performed at all flight conditions along the lines of that in Ref. 12 using the algorithm in Ref. 21. Equation (10) is equivalent to maximizing $\bar{\sigma}(\,)$ at each frequency of a given linear fractional transformation model with an uncertainty set $\Delta \in \mathbf{\Delta}_p$, as shown in Fig. 4,

$$\max_{\Delta \in \Delta_p} \bar{\sigma}[F_u(G_o|_\omega, \mathbf{\Delta})] \qquad (12)$$

where the upper linear transformation

$$F_u(G_o|_\omega, \Delta) = \left[G_{o22} + G_{o21}|_\omega \Delta (I - \Delta G_{o11}|_\omega)^{-1} G_{o12}|_\omega\right] \qquad (13)$$

$$y = F_u(G_o|_\omega, \Delta)$$

$$u = \left[G_{o22}|_\omega + G_{o21}|_\omega \Delta (I - \Delta G_{o11}|_\omega)^{-1} G_{o12}|_\omega\right] u \qquad (14)$$

The transfer function matrix $G_o|_\omega$ is partitioned as

$$G_o|_\omega = \begin{bmatrix} G_{o11}|_\omega & G_{o12}|_\omega \\ G_{o21}|_\omega & G_{o22}|_\omega \end{bmatrix}$$

The starting point in finding a solution to Eq. (12) is the one-parameter problem,[21] where $\mathbf{\Delta}_p := \{\delta I : -1 \leq \delta \leq 1\}$, that is, a single real, repeated perturbation is assumed. For this special case, Eq. (12) becomes

$$\max_{-1 \leq \delta \leq 1} \bar{\sigma}\left[G_{o22}|_\omega + G_{o21}|_\omega \delta (I - \delta G_{o11}|_\omega)^{-1} G_{o12}|_\omega\right] \qquad (15)$$

The one-parameter problem of Eq. (15) has a clear solution[21] described in Refs. 22 and 23. The one-parameter problem can easily be extended to the multiparameter case (11) as follows:

1) Initialize $\mathbf{\Delta}_p$ in Eq. (11) at midpoint (zero in this case).

2) Pick a random ordering of integers 1–9 (number of real uncertain parameters).

3) Hold all δ of $\mathbf{\Delta}_p$ fixed except the free element identified in step 2 and cycle through random ordering.

4) Maximize over $\mathbf{\Delta}_p$ using a single-parameter solution.

5) Set the value of the free element to the maximum value.

6) Repeat the steps for all δ of $\mathbf{\Delta}_p$.

The preceding algorithm is repeated over the entire frequency range, and Δ_ω is calculated; $\max_{G_i} \bar{\sigma}[(G_i - G_{o1})/G_{o1}]$ from criterion 1 and $\bar{\sigma}\{[G(\Delta_\omega) - G_o|_\omega]/G_o|_\omega\}\forall\omega$ from criterion 2 at all flight conditions can then be used to find the best operating point. In the case of a conflict between approaches 1 and 2, a judicious choice of operating point based on the frequency range of interest should be made. For the present case, with regard to approach 1, the plots of $\max_{G_i} \bar{\sigma}[(G_i - G_{o1})/G_{o1}]$ for all of the operating points G_{o1} are given in Fig. 5. Note that the smallest perturbations are with respect to the operating points of 35 and 45 m/s. Whereas the uncertainty ratio with respect to 35 m/s is at a minimum at the frequency range from 0.4 to 7 rad/s, the uncertainty ratio with respect to 45 m/s is at a minimum at the frequency range from 0.01 to 0.4 rad/s and again after 7 rad/s. With reference to Table 1, phugoid and short-period modes of all of the flight conditions are covered in the frequency range from 0.2 to 12 rad/s, and, hence, both flight conditions at 35 and 45 m/s are suited for controller design. However, with regard to criterion 2, it is found that the most sensitive operating speed to structured perturbations of the nature given in Sec. III.A is 45 m/s. In Fig. 5, $\bar{\sigma}\{[G(\Delta_\omega) - G_o|_\omega]/G_o|_\omega\}\forall\omega$ at 45 m/s is also shown. In summary, the operating speed of 45 m/s is the closest to other flight conditions and also the most sensitive to perturbations in aerodynamic derivatives. Therefore, the controller design is carried out at the cruise speed of 45 m/s.

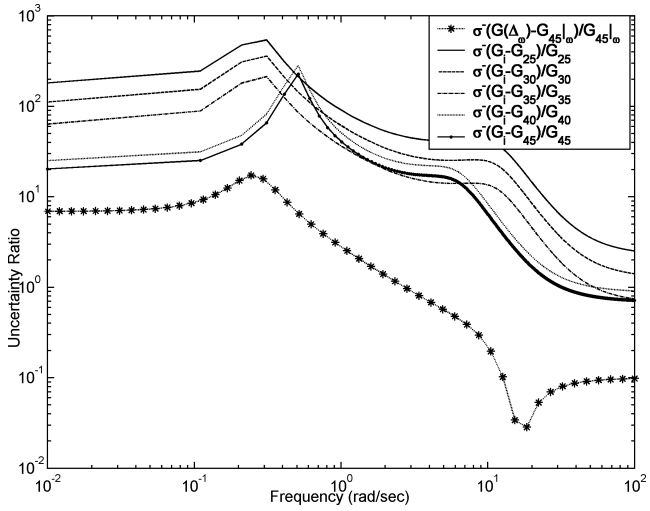

Fig. 5 Uncertainty ratios $\bar{\sigma}_{G_i}[(G_i - G_a)/G_a]$ and $\bar{\sigma}\{[G(\Delta_\omega) - G_{45}|_\omega]/G_{45}|_\omega\}\ \forall\ \omega$.

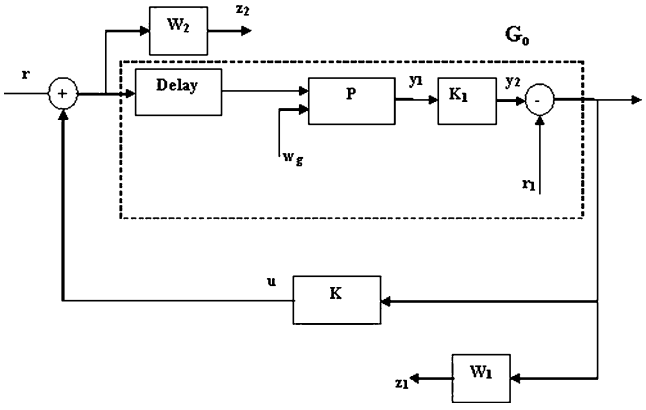

Fig. 6 H_∞ synthesis block diagram.

IV. H_∞ Synthesis Formulation and Closed-Loop Analysis

A. Formulation of H_∞ Synthesis

Based on the requirements presented in Sec. III.A, the H_∞ design synthesis model is chosen as in Fig. 6. In Fig. 6, P is nominal discrete-time aircraft model, including actuators, at the flight condition of 45 m/s. The sampling time is chosen as 20 ms to achieve synchronization with the PWM command signals from the ground. The command input from ground is r, and w_g is the longitudinal gust input. In Fig. 6, r_1 and w_g are treated as the exogenous input signals, z_1 and z_2 are the performance output signals, and $\boldsymbol{y}_2$ is the vector of measured outputs. K is the controller to be synthesized, and K_1 is the matrix of accelerometer and gyroscope sensitivities k_a and k_g:

$$K_1 = \begin{bmatrix} k_a & 0 \\ 0 & k_g \end{bmatrix}$$

A feedback path configuration is chosen for implementation because in forward path configuration the controller states need to be initialized depending on the reference inputs and actuator inputs during switchover from open-loop control to closed-loop control in flight. Whereas many switching strategies are reported in literature,[24,25] the states of the feedback path controller can be initialized to zero without resorting to these switching strategies.

The H_∞ design problem is to find a stabilizing controller K, such that

$$\|T_{zw}\|_\infty < \gamma \tag{16}$$

for a given γ. The T_{zw} is the closed-loop transfer function matrix between the exogenous input vector $\boldsymbol{w} = [r_1\ \ w_g]'$ and the performance output vector $\boldsymbol{z} = [z_1\ \ z_2]'$ given by

$$T_{zw} = \begin{bmatrix} W_1 S_o & W_1 S_o P_2 \\ W_2 S_i K & W_2 S_i K K_1 P_2 \end{bmatrix} \tag{17}$$

The condition $\|T_{zw}\|_\infty < 1$ can easily be extended to the case $\|T_{zw}\|_\infty < \gamma$ through scaling; $\|\varepsilon T_{zw}\|_\infty < 1$, where $\varepsilon = 1/\gamma$. The output and input sensitivity S_o and S_i are, respectively, given by

$$S_o = [I + K_1 P_1 K]^{-1}, \qquad S_i = [I + K K_1 P_1]^{-1} \tag{18}$$

$P_1(z) = \boldsymbol{y}_1(z)/\boldsymbol{u}(z)$ is the transfer function from controller input to the plant output and $P_2(z) = \boldsymbol{y}_1(z)/\boldsymbol{w}_g(z)$ is the transfer function from vertical gust input to the plant output. W_1, being the weighting function of the error due to wind disturbances and on output sensitivity S_o, is related to the performance requirements. W_1 is chosen to have low-pass filter characteristics, and its gain determines the bandwidth of disturbance rejection. W_2 is the weighting function on the control effort due to wind disturbances and reference signals $S_i K$ and $S_i K K_1 P_2$, respectively. Hence, W_2 is chosen to have high-pass filter characteristics. The gains of the control effort weighting function are chosen to avoid saturation of the elevator and thrust flap and to give more authority to elevator.

Given the state-space representation of the interconnection for the generalized plant (aircraft dynamics augmented with weighting matrices W_1 and W_2) in Fig. 6,

$$\begin{aligned} \boldsymbol{x}(k+1) &= A\boldsymbol{x}(k) + B_1\boldsymbol{w}(k) + B_2\boldsymbol{u}(k) \\ \boldsymbol{z}(k) &= C_1\boldsymbol{x}(k) + D_{11}\boldsymbol{w}(k) + D_{12}\boldsymbol{u}(k) \\ \boldsymbol{y}(k) &= C_2\boldsymbol{x}(k) + D_{21}\boldsymbol{w}(k) \end{aligned} \tag{19}$$

where $\boldsymbol{x}(k)$ is the state vector, $\boldsymbol{u}(k)$ is the control input vector, $\boldsymbol{y}(k)$ is the measurement vector, $\boldsymbol{w}(k)$ is the exogenous input vector, and $\boldsymbol{z}(k)$ is the output to be controlled. The algorithm from Ref. 13 derives an explicit state-space formula for a controller of the form

$$\begin{aligned} \boldsymbol{x}_c(k+1) &= A_c\boldsymbol{x}_c(k) + B_c\boldsymbol{y}(k) \\ \boldsymbol{u}(k) &= C_c\boldsymbol{x}_c(k) + D_c\boldsymbol{y}(k) \end{aligned} \tag{20}$$

that internally stabilizes the closed-loop system, such that $\|T_{zw}\|_\infty < 1$. The controller state, control, and measurement matrices A_c, B_c, C_c, and D_c are given in terms of the solutions of two discrete Ricatti equations subject to the following two conditions[13]:

1) Condition 1 states that system (A, B_2, C_1, D_{12}) has no invariant zeros on the unit circle and is left invertible.

2) Condition 2 states that system (A, B_1, C_2, D_{21}) has no invariant zeros on the unit circle and is right invertible.

The choice of weighting functions is based on the fulfillment of the conditions 1 and 2. The linearized aircraft model with actuators is discretized and augmented with computational delay and discretized weighting functions to obtain the generalized state-space representation of G_o in Fig. 6. Conditions 1 and 2 dictate that the weighting function W_2 be proper. The direct feedthrough term from control input to measurement D_{11} is zero because the linearized aircraft model is connected in series with a strictly proper actuator model [Eq. (2)].

B. Closed-Loop Analysis

The weighting function W_1 determines the performance properties of the closed-loop system. In other words, W_1^{-1} gives an upper bound on the sensitivity. The poles of the weighting function determine the bandwidth of disturbance rejection. The weighting function W_2 determines the robustness characteristics of the close-loop system to unstructured additive uncertainties; that is, W_2^{-1} acts as the upper bound on the controller gains $S_i K$. Also, the zeros of W_2 determine the actuator bandwidth and noise rejection properties. However, a large gain of W_2 results in less control activity and

sluggish response, and a large frequency zero will lead to reduced noise rejection properties. Hence, W_2 is chosen to strike a balance between robustness, satisfactory response, and good noise rejection.

When the preceding observations are into account, the final choice of weighting functions for W_1 and W_2 are

$$W_1 = \begin{bmatrix} w_{11} & 0 \\ 0 & w_{12} \end{bmatrix} = \begin{bmatrix} \dfrac{100}{5s+1} & 0 \\ 0 & \dfrac{100}{5s+1} \end{bmatrix} \tag{21}$$

$$W_2 = \begin{bmatrix} w_{21} & 0 \\ 0 & w_{22} \end{bmatrix} = \begin{bmatrix} \dfrac{0.02(s+1)^2}{(0.001s+1)^2} & 0 \\ 0 & \dfrac{(0.1s+1)^2}{(0.001s+1)^2} \end{bmatrix} \tag{22}$$

W_1 and W_2 are chosen to be strictly proper and proper, respectively, to satisfy conditions 1 and 2 (Sec. IV.A). The discrete form of weighting functions is then augmented with the discrete aircraft model. Functions w_{11} and w_{12} are chosen to be identical, implying equal weighting to both of the sensitivity channels; w_{21} corresponding to the elevator channel has lower gain than the thrust flap channel to give more authority to the elevator. Also, the thrust flap channel has higher frequency zeros than the elevator channel to aid in the high-frequency control effort. The resulting controller is of order 14, equal to the order of the generalized plant, and the limiting value of γ is 0.85. The order is reduced to five using the Hankel norm approximation. Furthermore, all pole–zero pairs with small residues are removed by observation to reduce the onboard computation time.

The reduced-order controller transfer function in the z domain is

$$K(z) = \begin{bmatrix} \dfrac{-0.014446(z-1.155)(z-1.02)(z-0.9866)}{(z-0.9962)(z^2-1.959z+0.9597)} & \dfrac{-0.0002397(z-1.236)(z^2-1.986z+0.9857)}{(z-0.999)(z-0.9961)(z^2-1.959z+0.9597)} \\ \dfrac{0.025647(z-1.067)(z^2-1.982z+0.9829)}{(z-0.9958)(z^2-1.959z+0.9597)} & \dfrac{0.00025081(z-0.9043)(z^2-2.008z+1.009)}{(z-0.999)(z-0.9958)(z^2-1.959z+0.9597)} \end{bmatrix}$$

The frequency responses of the individual full-order and final reduced-order controller transfer functions are shown in Fig. 7. The controller transfer functions exhibit properties of a low-pass filter in all channels, with the gain in the normal acceleration channel being lower than the gain in the pitch rate channel by 12 dB. This is because the open-loop gain in the pitch rate channel is lower than the normal acceleration channel by about 12 dB. The singular values of output sensitivity S_o, as defined in Eq. (18), is shown in Fig. 8 for all cruise speeds. The output sensitivity exhibits very small gains at frequencies up to 2 rad/s, after which it peaks and finally remains at 0 dB. This trend is observed at all cruise speeds except for the flight condition of 25 m/s, where the sensitivity peaks to 0.5 dB at 0.6 rad/s, which is negligible. However, it remains below 0 dB in the remaining region before settling to 0 dB at 10 rad/s. This implies that the low-frequency output disturbance rejection property of the closed-loop system is nearly preserved at all flight conditions. Also, a comparison of open-loop singular values and closed-loop sensitivity shows that the condition number of the open loop at an operating condition of 45 m/s is 1258.92 at 0.1 rad/s and 281.83 at 1 rad/s. In contrast, the condition number of sensitivity is 1.51 at 0.1 rad/s and 1.25 at 1 rad/s. These values indicate that the controllability of the closed loop has increased by 800 times compared to the open loop at 0.1 rad/s and 225 times at 1 rad/s. Figure 9 shows the sensitivity of control effort to input demands $S_i K$ for all cruise speeds. $S_i K$ determines the robustness of the closed-loop system to additive uncertainty and also the upper bounds on the controller gains. The control effort is small at high frequencies because the pilot command inputs are likely to contain only low-frequency signals. However, note that the peak value of $S_i K$ becomes larger as we move toward the cruise speed of 25 m/s. $S_i K$ determines robustness of the system with an additive uncertainty of the form

$$G(\Delta) = G_o + \Delta \tag{23}$$

where Δ is the frequency-dependent additive perturbation, G_o is the nominal plant, and $G(\Delta)$ is the perturbed system. In the present design, $\|S_i K\|_\infty = 0.4586$ for the cruise speed of 45 m/s. The corresponding gain margin excess $(\|S_i K\|_\infty)^{-1}$ is 6.77 dB, indicating good robustness. The value $\|S_i K\|_\infty$ increases to 0.87 or a gain margin excess of 1.2 dB for the flight condition of 25 m/s. Though this indicates deterioration in robustness, the closed-loop system at 25 m/s still exhibits a positive gain margin. The requirement of robustness to nominal time delays usually places a limitation on the

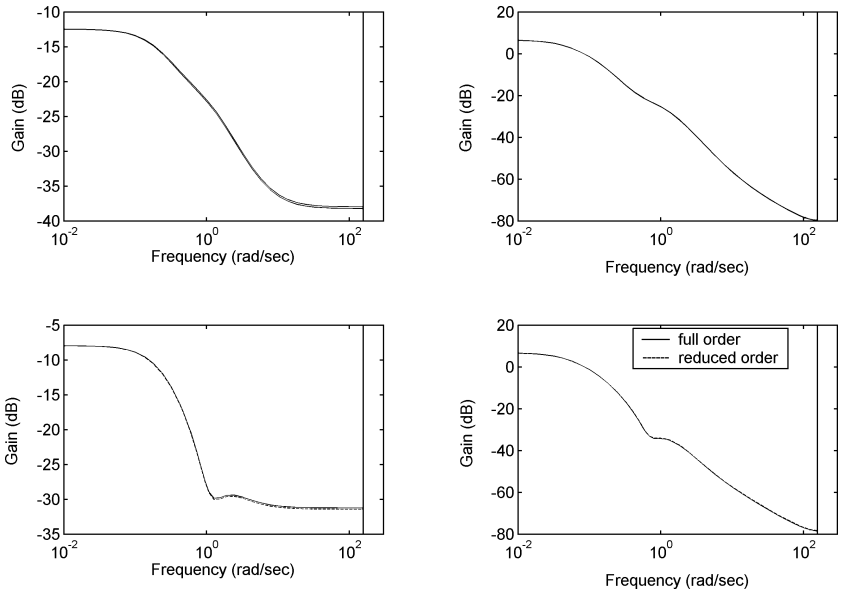

Fig. 7 Frequency response of full- and reduced-order controllers.

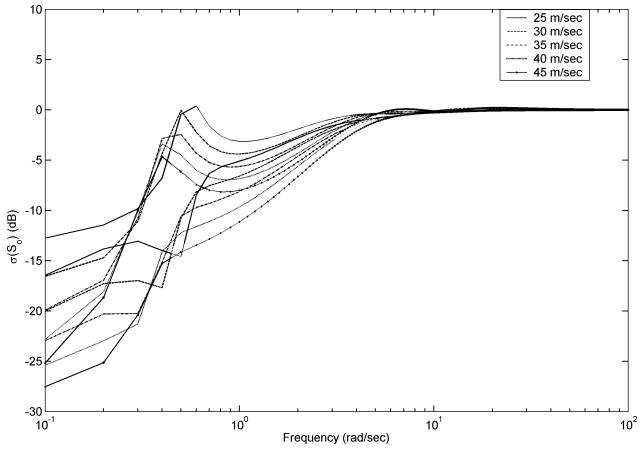

Fig. 8 Frequency response of output sensitivity S_o at different flight conditions.

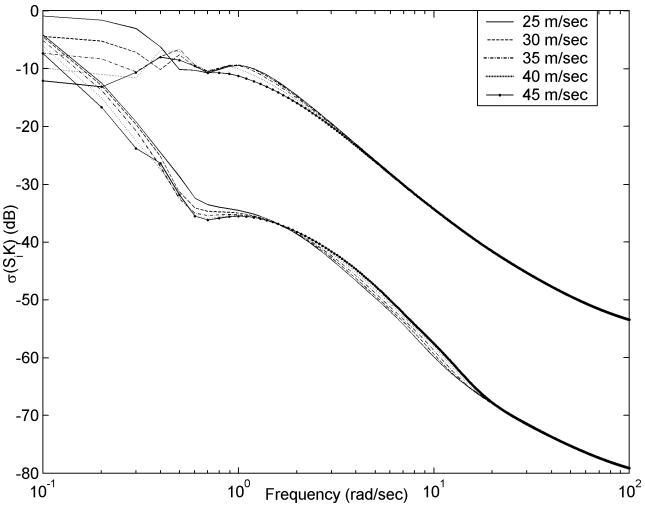

Fig. 9 Control effort S_iK at different flight conditions.

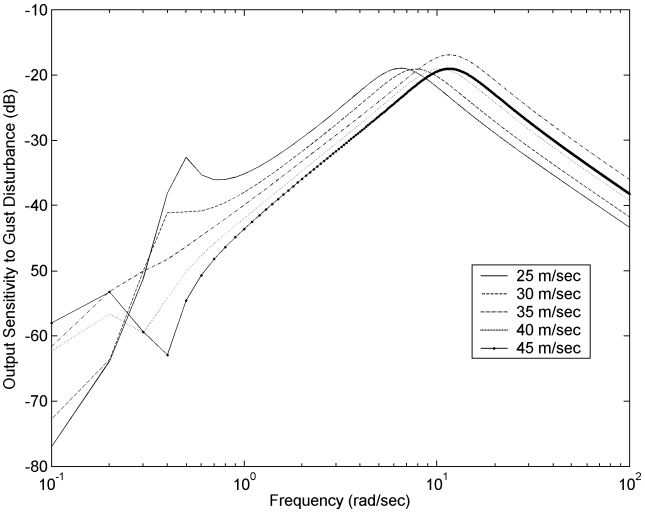

Fig. 10 Sensitivity of outputs to wind disturbances at different flight conditions.

achievable bandwidth of the system.[26] (This is similar to the limitation placed by right half-plane zero.) However, the effect of delays is not a concern in the present study because the corner frequency corresponding to delay (50 Hz) is much higher than the closed-loop bandwidth of 10 rad/s (Fig. 8).

Figure 10 shows the sensitivity of outputs to wind disturbances at all flight conditions. The frequency at which the peak values occur decreases with a decrease in cruise speed, and at 25 m/s, the peak occurs at 6 rad/s. However, the singular values are still below −15 dB up to 12 rad/s as required in specifications (well below 0 dB), implying good gust rejection properties. The preceding frequency response analyses show that a discrete controller is capable of meeting all specifications, including robustness.

1. *Closed-Loop Pole Locations*

The closed-loop phugoid and short-period pole locations in the w domain are given in Table 1 for all of the cruise speeds. Note that the phugoid damping of the closed loop at the design point of 45 m/s has improved to 0.63 from the open-loop damping of 0.275, whereas the phugoid frequency has decreased slightly from 0.27 to 0.215 rad/s. The closed-loop short-period damping also shows an improvement (0.488) compared to the open-loop damping (0.477), whereas the frequency is the same at 11.7 rad/s. All closed-loop poles show a similar trend and satisfy the phugoid and short-period specifications, except at the cruise speed of 25 m/s, which shows a phugoid damping of 0.48. This damping is, however, satisfactory, considering the following: 1) The states u and θ influencing the phugoid mode are fed back. 2) The extreme case in the operating range is represented by 25 m/s.

2. *μ Analysis*

Robustness of the closed-loop system to both structured aerodynamic parameter uncertainty and unstructured input multiplicative uncertainty of the actuator of the form given in Sec. II is determined through μ analysis.[27,28] The interconnection in Fig. 4 can also be used to pose the robust stability problem to uncertainties with a block diagonal structure. In the present case, the controller is assumed to be absorbed in G_o. Let G_o have the input–output representation

$$\begin{bmatrix} G_{o11} & G_{o12} \\ G_{o21} & G_{o22} \end{bmatrix}$$

The well-known robust stability criterion[27] states that the system $F_u(G_o, \boldsymbol{\Delta})$ in Fig. 4 is well posed and stable if and only if $\mu_{\Delta p}[G_{o11}(j\omega)] < 1\ \forall\omega$ for a given block-structured uncertainty $\boldsymbol{\Delta} \in \boldsymbol{\Delta}_p$, such that $\bar{\sigma}(\boldsymbol{\Delta}) \leq 1$. In the present case, $\boldsymbol{\Delta}_p$ has the block diagonal structure $\boldsymbol{\Delta}_p = \text{diag}([\delta_1, \delta_2, \delta_3, \ldots, \delta_{11})]$, $\delta_1, \delta_2 \in C$, and $\delta_3, \delta_4, \ldots, \delta_{11} \in R$. Here, δ_1 and δ_2 represent the uncertainty in the actuator model, whereas $\delta_3, \ldots, \delta_{11}$ represent the uncertainty in aerodynamic coefficients.

The stability robustness of the closed-loop system is tested using a μ analysis tool box for all five flight conditions, assuming that all perturbations act simultaneously. The μ bounds are shown Fig. 11 for all cruise speeds. Note from Fig. 11 that the peak μ value of 0.68 for the cruise speed of 25 m/s is the highest, indicating deterioration in terms of stability. This is quite natural because 25 m/s represents the extreme case in terms of variation from the nominal condition

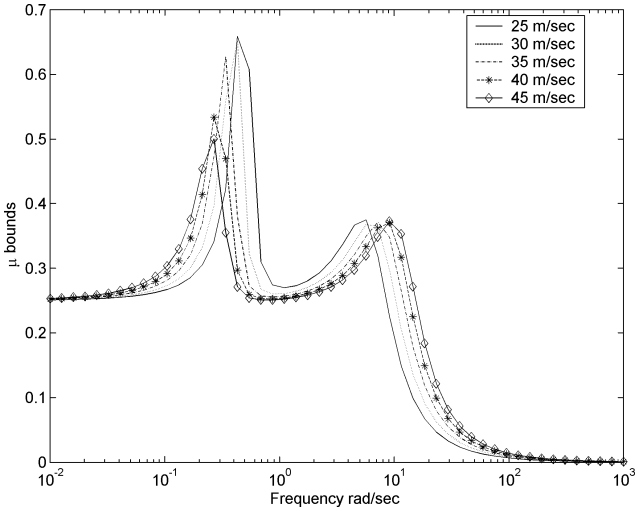

Fig. 11 Longitudinal robust stability μ bounds.

of 45 m/s. However, the bounds are still within the limit of one, indicating robust stability at all cruise speeds.

V. Simulation Results

A. Nonlinear Simulation

For the purposes of nonlinear simulation, flight simulation software called the Flight Analysis and Simulation Tool (FAST),[29] written in FORTRAN, is used. The program uses subroutines and library tools with a user-defined input file containing the vehicle parameters. The controller is used in the feedback loop and actuator models and a 0.02-s delay are included. The aircraft is first trimmed at straight and level flight at different speeds and at an altitude of 1200 m. The controller is switched on after 1 s. A 4-s duration positive pulse of amplitude 0.05 ms (about nominal trim pulse width), corresponding to a flap deflection of 1.9 deg, followed by a 4-s negative pulse, also of amplitude 0.05 ms (−1.9-deg flap deflection) is given at the acceleration command channel. This corresponds to the pilot moving the joystick on the ground from the trim point to one side and then to the other end and back. To simulate turbulence, a wideband white noise is filtered through discrete shaping filters derived from the Dryden spectra (see Ref. 15) in Eq. (5). To simulate sensor noise, white noise is passed through a high-pass first-order discrete shaping filter, given in continuous time as $[0.02(s+30)]/(s+100)$. The filter output is added to the sensed outputs of pitch rate and normal acceleration. Figure 12 shows the responses of pitch rate and angle of attack for all flight conditions. Total pitch angle and normal acceleration, as well as the open-loop response at 45 m/s are shown in Fig. 13. Figure 14 shows the total velocity response and elevator deflections, and Fig. 15 shows the thrust flap and command signals. From Figs. 13 and 14, note that the low-frequency disturbance effects are lower in the closed-loop response, which shows that in the presence of a controller gust disturbance, rejection is achieved. This property is retained at all flight conditions, which proves that the controller is robust in terms of disturbance rejection as is expected. Also, the closed-loop responses are fast and well damped for all of the flight conditions. A comparison of the open and closed loops indicates that whereas the open-loop phugoid states are still oscillatory, the closed-loop phugoid states are fast and well damped with a settling time of 6 s. The short-period states of pitch rate and angle of attack have a settling time of 4 s in the closed loop, whereas the open-loop responses remain oscillatory. These observations conform with the design requirement of improving the closed-loop damping while retaining the speed of response. Another observation is that the noise injected at the measurement channels is also rejected, a property also maintained at all flight conditions. The responses show that the requirement of robustness to time delay is also satisfied. In fact, simulation

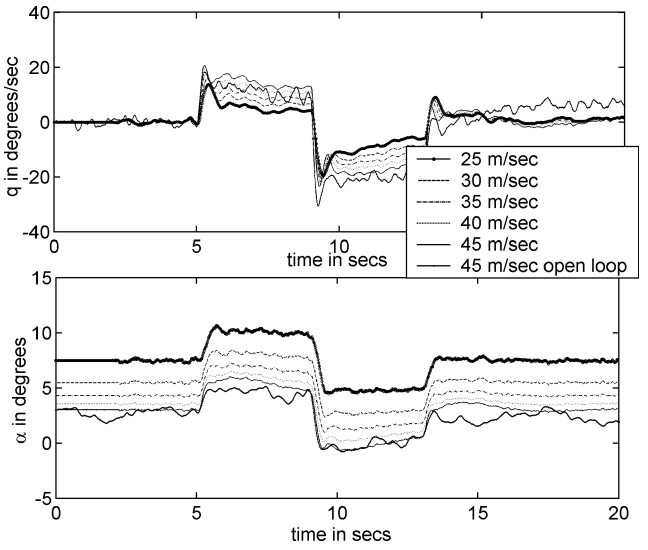

Fig. 12 Pitch rate and angle of attack response at all speeds and open-loop response at 45 m/s.

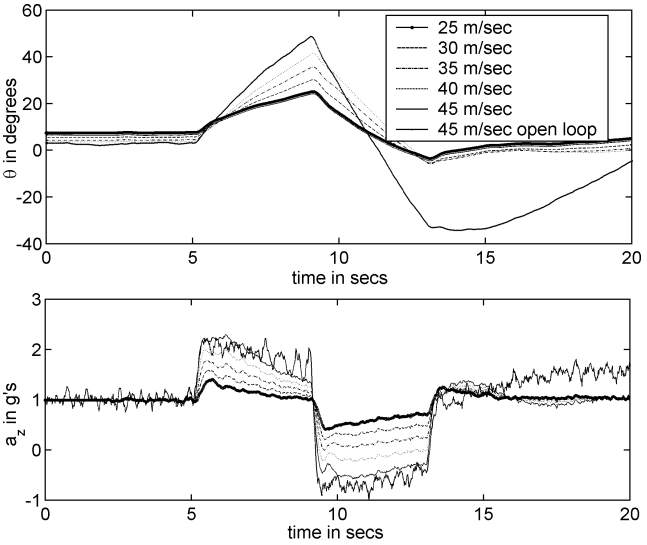

Fig. 13 Pitch angle and normal acceleration response of closed-loop system at all cruise speeds and open-loop system at 45 m/s.

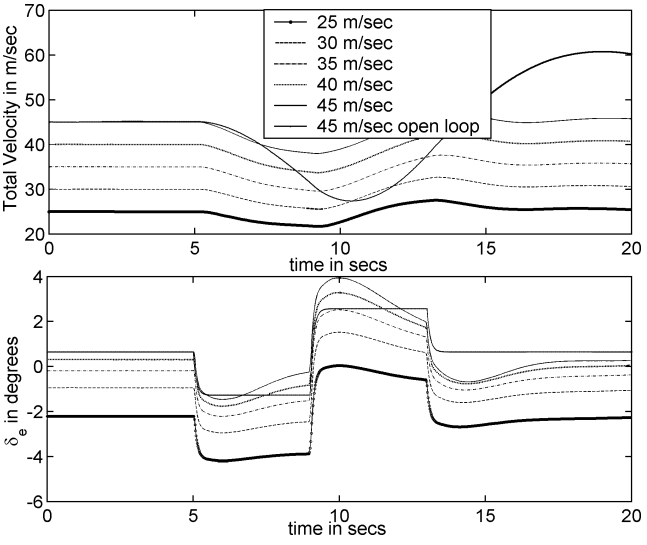

Fig. 14 Total velocity and elevator deflection of the closed-loop system at all cruise speeds and open-loop system at 45 m/s.

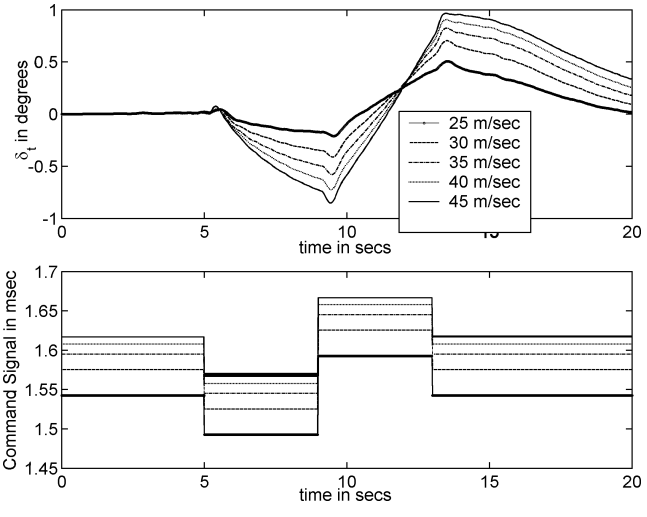

Fig. 15 Thrust flap deflection and command signal.

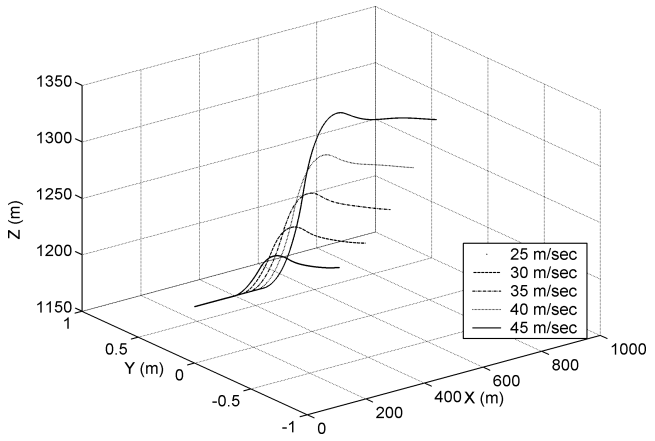

Fig. 16 Trajectory of aircraft at all flight conditions.

results (not shown) indicate that time delay up to three times the sampling time (Ts), that is, 0.06 s, does not degrade the performance of the closed-loop system.

The control surface deflections show that the ratio of thrust flap deflection to elevator deflection varies from 35% at 45 m/s to 32% at 25 m/s. Ideally, the control authority of thrust vectoring should be increased with a decrease in speed. This is especially true for full-scale thrust-vectored aircraft in which the jet exit momentum increases with decrease in speed. An inner-loop control allocation scheme using dynamic inversion[9] could compensate for the loss in control allocation. However, this aspect is not explored in the present study because the exit momentum remains almost constant with speed as mentioned in Sec. II. The trajectories traced by the aircraft at all speeds are shown in Fig. 16. Figure 16 basically means that the aircraft climbs up to an altitude ranging from 30 m at 25 m/s to 100 m at 45 m/s when the stick is pulled and held and climbs down when pushed in the opposite direction, finally leveling itself when the stick is brought back to trim position. Note that the trajectory is smooth with no oscillations, which is desirable from the pilot's point of view.

B. HILS

A functional HILS is performed by using a dSPACE DS1104 controller board, which is a real-time control system based on a floating-point processor running at 250 MHz. DS1104 features a graphical user interface for managing the controller card and a real time interface between Simulink® and dSPACE hardware. Real time code is built and implemented on the fixed-point motor control DSP TMS320LF2407A from Texas Instruments. The DSP is housed in a fight instrumentation card (FIC) developed in-house.

HILS provides a cost-effective means of testing the FIC (with the coded controller) and the control surfaces, namely, the elevator and thrust flap. The importance of testing control surface deflection in real time stems from the fact that the servos powering the control surfaces are connected to them through wires that can introduce many non-linearities like backlash and a dead zone. Also, the hinges of the control surfaces can introduce friction that has not been modeled. Control surface deflection and rate saturation can also be monitored in this setup. The interconnection diagram for HILS is shown in Fig. 17. PWM command signals from the remote transmitter are captured by the PWM capture unit of the DSP through the receiver (point 1). The signal is passed through a first-order low-pass filter with a frequency of 100 rad/s (point 2) to suppress noise. The inputs to the controller are simulated sensor outputs through an A/D converter, with units in volts, corresponding to the accelerometer and rate gyroscope, and the output of the controller is the pulse width (milliseconds). The control signal from the DSP is sent to the dSPACE 1104 PWM capture unit, and 1.6 ms is subtracted at the input of the actuator to account for the fact that a linear model is simulated. A saturation block is included in the DSP program to limit the control signal to 1.0–2.2 ms (point 3). The transport delay shown at point 4 is indicative of the fact that the control signal at any time instant is based on the measurement signal at the previous

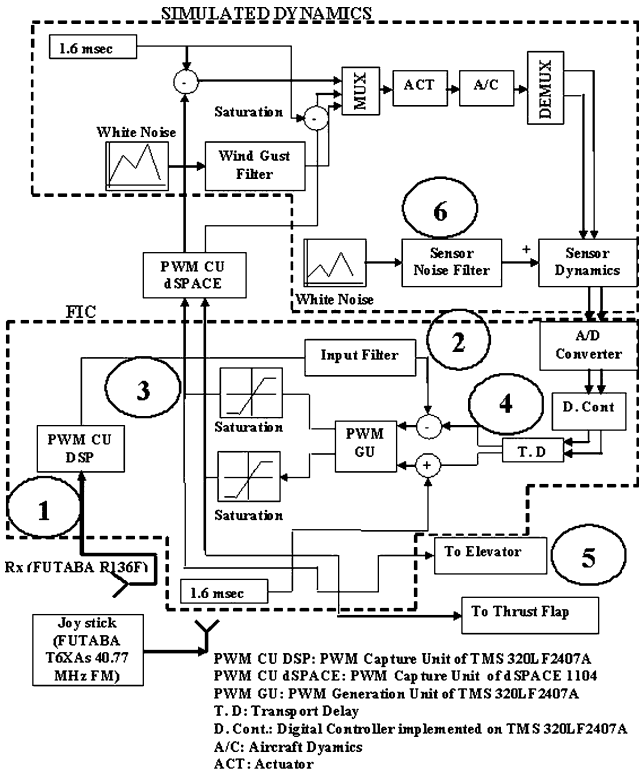

Fig. 17 Interconnection setup for HILS.

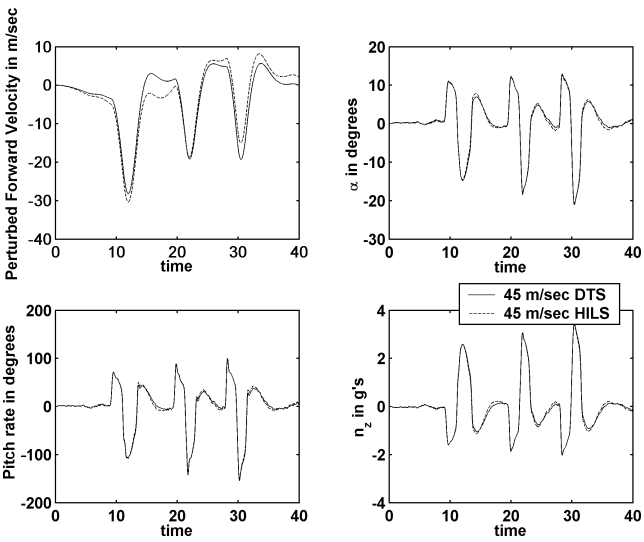

Fig. 18 Closed-loop responses of HILS and DTS.

time instant. The first control signal corresponding to the elevator is then sent to the elevator after adding 1.6 ms. A PWM signal of width 1.6 ms is added to the second feedback signal from the controller before being sent to the thrust flap servo for reasons similar to those already mentioned (point 5). The control surface deflections are checked for correctness of direction and saturation. Noise and gust disturbance are also injected at the simulated sensor outputs and plant input to check for control surface chattering (point 6).

After the simulation is started, the joystick in the transmitter is moved to one end and held for some time. The joystick is then again moved to the other end and held, after which it is brought back to the neutral position, and this pattern is repeated. To compare the results of the HILS, the same command signals are used in a desktop simulation (DTS) without any hardware. The time responses of both of the closed-loop systems are shown in Figs. 18 and 19.

The input command signals captured in the FIC do not contain any high-frequency noise due to the presence of a low-pass filter,

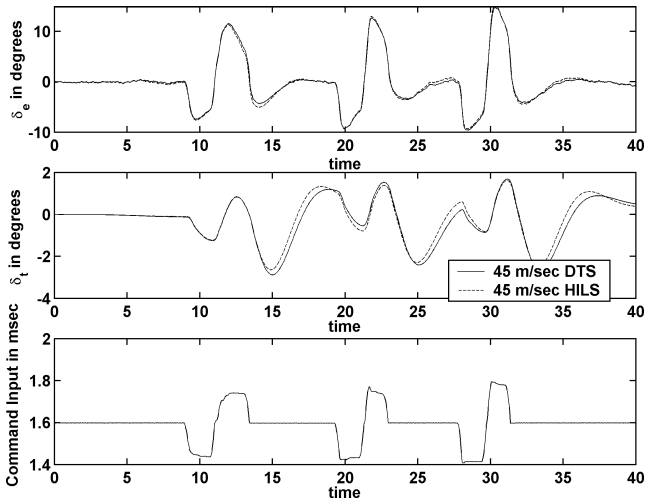

Fig. 19 Normal acceleration and control surface deflections of HILS and DTS.

at input. In fact, without the low-pass filter, the noise levels were observed to be high. The response from HILS is seen to be well damped and fast. The noise and disturbances injected at the sensor gain block and gust input point are rejected fully. No chattering is observed in the control surfaces at any instant as can be seen from the control surface deflections. Figures 18 and 19 also show that there is a slight mismatch in the responses between DTS and HILS, possibly due to fixed-point calculations in the DSP. The variables that show the highest deviation from DTS in terms of response are u (perturbed forward speed) and δ_t (thrust flap deflection). The highest difference between DTS and HILS for u is 4 m/s, whereas the maximum difference for δ_t is 0.4 deg. The control surface deflection of the elevator to the thrust flap is reduced to 0.32, as opposed to 0.35 in the nonlinear simulations and DTS. These differences can, however, be considered safe because typical pilot inputs are much lower than the reference signals given in HILS. Also, the HILS results show excellent robustness properties in spite of the computation delays encountered in DSP.

VI. Conclusions

This study describes a discrete longitudinal H_∞ stability augmentation system for a thrust-vectored unmanned aircraft in the entire cruise envelope. A single controller is designed to avoid gain scheduling. It is shown that a systematic approach to selection of the operating point for controller design provides good performance in the entire cruise envelope. Both structured and uncertain uncertainties are used for testing the robustness of the closed-loop system, and the single controller is shown to satisfy robustness criteria at all cruise speeds.

Extensive nonlinear simulations and functional HILS based on a dSPACE DS1104 controller board and Texas Instruments TMS320LF2407A, with gust and sensor noise, show that the closed-loop system exhibits very good gust and sensor noise rejection properties with excellent matching with the DTS. The simulation results show that H_∞ control can be successfully used in the design of flight controllers for unmanned aircraft.

Appendix: Model Parameters of RA

Longitudinal aerodynamic variables in polynomial form[30] are

$$C_L(\alpha, \delta_e, \delta_{IB}, \delta_t) = -0.0502 + 0.0071\delta_e + 0.00128\delta_t$$

$$C_D(\alpha, \delta_e, \delta_{IB}, \delta_t) = 0.0203 - 0.0015\alpha + 0.00047\alpha^2 - 0.00023\delta_e + 0.000033\delta_e^2 + 0.00013\alpha\delta_e + 0.00067\delta_t$$

$$C_m(\alpha, \delta_e, \delta_{IB}, \delta_t) = 0.0084 - 0.0021\alpha - 0.0026\delta_e - 0.1126\delta_t + 0.0067\delta_t\alpha - 0.0012\delta_t\alpha^2 + 0.0001\delta_t\alpha^3 \quad \text{(A1)}$$

Table A1 Model parameters of RA

Parameter	Value
Wing airfoil	NACA 63A006 mean line 230
Wingspan	1.09 m
Wing area	0.68 m^2
Geometric mean chord	0.747 m
Vertical tail airfoil	NACA 63A010
Fuselage length	1.49 m
Fuselage maximum diameter	0.13 m
Nozzle flap airfoil	NACA 63A010
Nozzle flap chord	0.11 m
Nozzle flap width	0.125 m
Takeoff weight	5.5 kg
I_{yy}	0.5182 kgm^2
I_{zz}	0.7232 kgm^2
I_{xx}	0.1583 kgm^2
I_{xz}	0.03144 kgm^2
Static thrust	32.54 N
Takeoff speed	~22 m/s
Landing speed	~20 m/s

Table A2 Trim parameter values

Speed, m/s	Angle of attack, deg	Elevator deflection, deg	Lift coefficient	Drag coefficient
25	7.4	−2.2	0.22	0.05
30	5.5	−0.9	0.16	0.04
35	4.3	−0.19	0.11	0.03
40	3.5	0.3	0.08	0.03
45	3.0	0.6	0.07	0.02

where C_L is the lift coefficient, C_D is the drag coefficient, C_m is the moment coefficient defined with respect to the center of gravity, α is the angle of attack in degrees, δ_e is the outboard elevon deflection in degrees, and δ_t is the thrust flap deflection in degrees.

The state-space representation of RA dynamics at 45 m/s at 1200-m altitude is

$$\begin{bmatrix} \dot{u} \\ \dot{\alpha} \\ \dot{q} \\ \dot{\theta} \end{bmatrix} = \begin{bmatrix} -0.1577 & -3.3168 & 0 & -9.802 \\ -0.0095 & -6.9513 & 0.9702 & 0 \\ 0 & -109.875 & -4.1492 & 0 \\ 0 & 0 & 1 & 0 \end{bmatrix} \begin{bmatrix} u \\ \alpha \\ q \\ \theta \end{bmatrix} + \begin{bmatrix} -1.9461 & -3.7601 \\ -1.1975 & -0.2160 \\ -156.4535 & -111.1232 \\ 0 & 0 \end{bmatrix} \begin{bmatrix} \delta_e \\ \delta_t \end{bmatrix} \quad \text{(A2)}$$

The various model parameters of RA are given in Table A1 and trim parameter values for straight and level flight at different speeds are given in Table A2.

Acknowledgments

The authors thank S. P. Govindaraju and V. Surendranath, Department of Aerospace Engineering, Indian Institute of Science; Seetharama Raju and Girish Dixit, Aeronautical Development Agency, Bangalore; and Shyam Shetty and Girish Deodhare, National Aerospace Laboratories, Bangalore, for their valuable comments and suggestions during the course of this work. The authors also thank the anonymous reviewers for their comments that have improved the quality of this paper.

References

[1]Ostroff, A. J., and Proffitt, M. S., "Longitudinal Control Design—Approach for High Angle of Attack Aircraft," NASA TP-3302, Feb. 1993.

[2]Wichman, K. D., Pahle, J. W., Bahm, C., Davidson, J. B., Bacon, B. J., Murphy, P. C., Ostroff, A. J., and Hoffler, K. D., "High-Alpha Handling Qualities Flight Research on the NASA F/A-18 High-Alpha Research Vehicle," NASA TM-4773, Nov. 1996.

[3]Kempel, R. W., and Michael, R. E., "Flight Control Systems Development and Flight Test Experience with HiMAT Research Vehicles," NASA TP-2822, June 1988.

[4]Govinda Raju, S. P., Reddy, K. R., Srinivasa Rao, B. R., Surendranath, V., and Khamesra, N., "A Study of Thrust Vectoring on a Remotely Piloted Model Airplane," Dept. of Aerospace Engineering, Rept. IWTR 277, Indian Inst. of Science, Bangalore, India, May 2001.

[5]Hyde, R. A., *H_∞ Aerospace Control Design, A VSTOL Flight Application*, Springer-Verlag, Berlin, 1995, pp. 125–198.

[6]Haiges, K. R., "Robust Control Law Development for Modern Aerospace Vehicles," NASA Ames Research Center, Rept. WL-TR-91-3105, Moffett Field, CA, Aug. 1991.

[7]Adams, R. J., Buffington, J. M., Sparks, A. G., and Banda, S. S., *Robust Multivariable Flight Control*, Springer-Verlag, London, 1994.

[8]Adams, R. J., Buffington, J. M., and Banda, S. S., "Design of Nonlinear Control Laws for High-Angle-of-Attack Flight," *Journal of Guidance, Control, and Dynamics*, Vol. 17, No. 4, 1994, pp. 737–746.

[9]Reigelsperger, W. C., and Banda, S. S., "Nonlinear Simulation of a Modified F-16 with Full Envelope Control Laws," *Control Engineering Practice*, Vol. 6, No. 3, 1998, pp. 309–320.

[10]Tucker, M. R., and Walker, D. J., "An H_∞ Approach," *Robust Flight Control: A Design Challenge*, edited by J. F. Magni, S. Bennani, and J. Terlouw, Lecture Notes in Control and Information Sciences, Springer-Verlag, 1997, Chap. 21.

[11]Kannan, N., and Seetharama Bhat, M., "Design of Discrete H_∞ Longitudinal Controller for a Research Aircraft," *Proceedings of the 26th National Control Conference*, Systems Society of India, Hyderabad, India, 2002, pp. 284–299.

[12]Shin, J. Y., Balas, G. J., and Packard, A. K., "H_∞ Control of the V 132 X-38 Lateral–Directional Axis," *Proceedings of the American Control Conference*, Vol. 2, American Automatic Control Council, Dayton, OH, 2000, pp. 1862–1866.

[13]Stoorvogel, A. A., *The H_∞ Control Problem*, Prentice–Hall, London, 1992, pp. 190–204.

[14]Govinda Raju, S. P., Reddy, K. R., Srinivasa Rao, B. R., and Surendranath, V., "Experimental Study of Aerodynamic Forces and Moment Characteristics in the Wind Tunnel on an Aircraft Model with Thrust Vector Control in Pitch and Yaw Directions," Dept. of Aerospace Engineering, Rept. IWTR 278, Indian Inst. of Science, Bangalore, India, April 2000.

[15]Schmidt, L. V., *Introduction to Aircraft Flight Dynamics*, AIAA Education Series, AIAA, Reston, VA, 1998, pp. 165–198.

[16]Roskam, J., *Airplane Design, Part VI: Preliminary Calculations of Aerodynamic, Thrust and Power Characteristics*, Roskam Aviation and Engineering Corp., Ottawa, KS, 1970, pp. 371–490.

[17]Amato, F., Ciniglio, U., Corrato, F., and Iervolino, R., "μ Synthesis for a Small Commercial Aircraft: Design and Simulator Validation," *Journal of Guidance, Control, and Dynamics*, Vol. 27, No. 3, 2004, pp. 479–490.

[18]Cooper, G. E., and Harper, R. P., Jr., "The Use of Pilot Rating in the Evaluation of Aircraft Handling Qualities," NASA TN D-5153, April 1969.

[19]"Flying Qualities of Piloted Airplanes," MIL-SPEC MIL-F-8785C, U.S. Government Printing Office, Washington, DC, Nov. 1980.

[20]"Flying Qualities of Piloted Aircraft," MIL-STD-1797A, U.S. Dept. of Defense, Washington, DC, Jan. 1990.

[21]Packard, A., Balas, G., Liu, R., and Shin, J. Y., "Results on Worst-Case Performance Assessment," *Proceedings of the American Control Conference*, American Automatic Control Council, Dayton, OH, 2000, pp. 2425–2427.

[22]Boyd, S., Balakrishnan, V., and Kabamba, P., "A Bisection Method for Computing the H_∞ Norm of a Transfer Matrix and Related Problems," *Math Control Signals and Systems*, Vol. 2, No. 3, 1989, pp. 207–219.

[23]Bruinsma, N., and Steinbunch, M., "A Fast Algorithm to Compute the H_∞ Norm of a Transfer Function Matrix," *Systems and Control Letters*, Vol. 14, No. 4, 1990, pp. 287–293.

[24]Astrom, K. J., and Wittenmark, B., *Computer Controlled Systems—Theory and Design*, Prentice–Hall, Englewood Cliffs, NJ, 1984, pp. 361–394.

[25]Hanus, R., Kinnaert, M., and Henrotte, J. L., "Conditioning Technique, a General Anti-Windup and Bumpless Transfer Method," *Automatica*, Vol. 23, No. 6, 1987, pp. 729–739.

[26]Seron, M. M., Braslavsky, J. H., and Goodwin, G. C., *Fundamental Limitations in Filtering and Control*, Springer-Verlag, London, 1997, pp. 47–117.

[27]Packard, A., and Doyle, J., "The Complex Structured Singular Value," *Automatica*, Vol. 29, No. 1, 1992, pp. 71–109.

[28]Balas, J. G., Doyle, J., Glover, K., Packard, A., and Smith, R., "μ Analysis and Synthesis Toolbox," MathWorks Inc., Natick, MA, URL: http://www.mathworks.com/access/helpdesk/help/toolbox/mutools [cited 10 Aug. 2004].

[29]Pashilkar, A. A., "FAST User's Manual Version 0.1, NAL PD FC 0314," Flight Mechanics and Control Div., National Aerospace Labs., Bangalore, India, Sept. 2003.

[30]Govinda Raju, S. P., Reddy, K. R., Srinivasa Rao, B. R., Surendranath, V., and Khamesra, N., "Aerodynamic Modelling of a Thrust-Vectoring Aircraft in the Longitudinal Plane," Dept. of Aerospace Engineering, Rept. IWTR 279, Indian Inst. of Science, Bangalore, India, April 2000.